COMMUNICATIONS IN COMPUTATIONAL PHYSICS
Vol. **4**, No. 5, pp. 1194-1215

Commun. Comput. Phys.
November 2008

A Kinetic-Hydrodynamic Simulation of Liquid Crystalline Polymers Under Plane Shear Flow: 1+2 Dimensional Case†

Guanghua Ji[1], Haijun Yu[2] and Pingwen Zhang[3,*]

[1] *Laboratory of Mathematics and Complex Systems, Ministry of Education and School of Mathematical Sciences, Beijing Normal University, Beijing 100875, China.*
[2] *School of Mathematical Sciences and CCSE, Peking University, Beijing 100871, China.*
[3] *LMAM, School of Mathematical Sciences and CCSE, Peking University, Beijing 100871, China.*

Received 4 March 2008; Accepted (in revised version) 20 July 2008

Available online 9 September 2008

Abstract. We consider the extended Doi model for nematic liquid crystalline polymers in-planar shear flow, which is inhomogeneous in shear direction. We study the formation of microstructure and the dynamics of defects. We discretize the Fokker-Plank equation using the spherical harmonic spectral method. Five in-plane flow modes and eight out-of-plane flow modes are replicated in our simulations. In order to demonstrate the validity of our method in simulating liquid crystal dynamics, we replicated weak shear limit results and detected defects. We also demonstrate numerically that the Bingham closure model, which maintains energy dissipation, is a reliable closure model.

PACS: 61.30.Dk, 61.30.Jf, 64.70.mf

Key words: Non-local potential, anchoring condition, spherical harmonic, kinetic-hydrodynamic, defects, Bingham closure.

1 Introduction

The nematic phase is one of the "simplest" liquid crystal phases known, for which an orientational order exists [1]. Most of the hydrodynamic theories formulated for liquid crystalline polymers(LCPs) are based on rod-like molecules, including the well known Leslie-Eriksen (**LE**) theory [2], developed to describe low molecular weight nematic liquid crystals, the Doi kinetic theory [3] and a variety of tensor-based theories, such as

†Dedicated to Professor Xiantu He on the occasion of his 70th birthday.
*Corresponding author. *Email addresses:* ghji@bnu.edu.cn (G. Ji), pzhang@pku.edu.cn (P. Zhang)

Hand's theory [4], Beris and Edwards' theory formulated through Poisson brackets [5], and Tsuji and Rey's phenomenological theory [6]. The **LE** theory was popular in simulations of LCPs for its simplicity. However, the **LE** theory predicts flow aligning and tumbling, but fails to catch defects, where the director cannot be defined. The Doi kinetic theory for spatially homogeneous flows of rod-like molecules has been successfully used to describe the rheological behavior of liquid crystalline polymers [3]. Abundant phenomena, such as tumbling, wagging, flow-aligning and logrolling, were predicted using the Doi model (Marrucci and Maffettone [7], Larson [8], Larson and Öttinger [9] and Nayak [10]). Faraoni [11], Forest et al. [12, 13] and others studied the Doi model in detail using spherical harmonic analysis, and generated the detailed phase diagram. Wang [14] extended the model to disc-shaped molecules by introducing a shape parameter $\alpha=\frac{r^2-1}{r^2+1}$, with the molecular aspect ratio r.

Liquid crystalline flows are characterized by the presence of three important effects: (1) short range order elasticity, (2) long range order elasticity, and (3) viscous flow. The **LE** theory addresses the long range order elasticity and viscous flow effects, while the Doi theory focuses on the short range order elasticity and the flow effect. Marrucci and Greco [15] extended the classical Maier-Saupe potential to the spatial inhomogeneous case, which accounts for spatial distortional elasticity. Wang [14] extended the Kuzuu and Doi theory to flowing systems of nonhomogeneous LCPs using an estimate of the Marrucci-Greco potential, and the shape parameter α. Fend et al. [16] adopted a one-constant Marrucci-Greco potential. Wang et al. [17] introduced a kernel type potential to describe the molecular interaction, and introduced an extra term in the form of an elastic body force. The Marrucci-Greco potential can be derived by local expansion, and the classical Ericksen-Leslie equations can be derived in the small Deborah number limit [18]. Rey and Tsuji [19] studied the complete tensor model [5] in detail, and showed the sketch of rheological phase diagram as a function of the ratio of short to long rang elasticity and the ratio of viscous flow to long rang elasticity effects, which is known as Ericksen number.

We apply the extended model to planar shear flow including kernel type potential and spatial diffusion term, which plays an important role in defect dynamics [20]. The paper is organized as follows. First, we present the extended kinetic-hydrodynamic model. In Section 3, we introduce the numerical scheme of LCPs imposed under shear flow. In Section 4, we show our numerical results including flow modes, dynamics of defects, weak shear limit results. A comparison among complete closure model, Bingham closure model, 1+1 kinetic model and our 1+2 kinetic model is given at the end of this section. Finally, we discuss the validity of this work.

2 The extended model

The extended Doi kinetic theory for inhomogeneous flow of rod-like LCPs can be specified by the following Smoluchowski equation:

$$\frac{\partial f}{\partial t}+\mathbf{v}\cdot\nabla f=\nabla\cdot\left\{[D_{\|}\mathbf{mm}+D_{\perp}(\mathbf{I}-\mathbf{mm})]\cdot(\nabla f+\frac{1}{k_BT}f\nabla U)\right\}$$
$$+D_r\mathcal{R}\cdot\left(\mathcal{R}f+\frac{1}{k_BT}f\mathcal{R}U\right)-\mathcal{R}\cdot(\mathbf{m}\times\kappa\cdot\mathbf{m}f), \tag{2.1}$$

where $D_{\|}\geq 0$ and $D_{\perp}\geq 0$ are the translational diffusion coefficients parallel and normal to the orientation of the LCP molecule and D_r is the rotational diffusivity for an isotropic solution. $\mathcal{R}=\mathbf{m}\times\frac{\partial}{\partial\mathbf{m}}$ is the gradient operator on the unit sphere S^2, $\kappa=(\nabla\mathbf{v})^T$ is the transpose of the velocity gradient, k_B is the Boltzman constant, and T is the absolute temperature. Here, the nonlocal intermolecular potential:

$$U(\mathbf{x},\mathbf{m},t)=k_BT\int_{\Omega}\int_{\|\mathbf{m}'\|=1}B(\mathbf{x},\mathbf{m};\mathbf{x}',\mathbf{m}')f(\mathbf{x}',\mathbf{m}',t)d\mathbf{m}dt, \tag{2.2}$$

introduces the long-range order elasticity, arising from spatial gradients of the orientational order. The Marrucci-Greco potential can be derived by local expansion of $f(\mathbf{x}',\mathbf{m}',t)$ at $\mathbf{x}$.

The Navier-Stokes type equations for macro incompressible flow are

$$\rho\frac{d\mathbf{v}}{dt}+\nabla\cdot p=\eta_s\Delta\mathbf{v}+\nabla\cdot\tau_p+\mathbf{F}^e, \tag{2.3}$$
$$\nabla\cdot\mathbf{v}=0, \tag{2.4}$$

where $\mathbf{F}^e=\langle\nabla U\rangle$ is the body force induced by the long-range molecular interaction [17], p is the static pressure and τ_p is the LCP viscoelastic stress,

$$\tau_p=2k_BT\nu\xi_r\mathbf{D}:\langle\mathbf{mmmm}\rangle-\langle\mathbf{mm}\times(k_BT\frac{\mathcal{R}f}{f}+\mathcal{R}U)\rangle. \tag{2.5}$$

Here, $\mathbf{D}=(\kappa+\kappa^T)/2$ and

$$\langle(\cdot)\rangle=\int_{|\mathbf{m}|=1}(\cdot)f(\mathbf{m},x,t)d\mathbf{m}.$$

The micro and macro equations coupled with each other by τ_p, $\mathbf{F}^e$ and κ. We refer the reader to [17, 18] for more detail.

2.1 Dimensionless equations

We take the macro velocity V to be the characteristic velocity, and the length of the macro domain L to be the characteristic length. Then the approximate characteristic time is L/V. Based on this choice of scales, the dimensionless equations for the coupled model

(2.1)-(2.5) can be written as

$$\frac{\partial f}{\partial t}+\nabla\cdot(\mathbf{v}f)=\frac{\varepsilon^2}{De}\nabla\cdot\{[D_\perp(\mathbf{I}-\mathbf{mm})+D_\parallel\mathbf{mm}]\cdot(\nabla f+f\nabla U)\}$$
$$+\frac{1}{De}\mathcal{R}\cdot(\mathcal{R}f+f\mathcal{R}U)-\mathcal{R}(\mathbf{m}\times\kappa\cdot\mathbf{m}f), \tag{2.6}$$
$$\frac{\partial\mathbf{v}}{\partial t}+(\mathbf{v}\cdot\nabla)\mathbf{v}=\frac{1-\gamma}{Re}\Delta\mathbf{v}-\nabla p+\frac{\gamma}{ReDe}(\nabla\cdot\tau^p+\mathbf{F}^e), \tag{2.7}$$
$$\nabla\cdot\mathbf{v}=0, \tag{2.8}$$
$$\tau^{(p)}_{\alpha\beta}=3S_{\alpha\beta}-\langle(\mathbf{m}\times\mathcal{R}U)_\alpha m_\beta\rangle+\frac{De}{2}\kappa_{kl}\langle m_\alpha m_\beta m_k m_l\rangle, \tag{2.9}$$
$$S_{ij}=\langle m_i m_j-\frac{1}{3}\delta_{ij}\rangle.$$

The Deborah number De is defined as $De=\frac{V/L}{D_r}$, which is the ratio of relaxation time and macro scale time, and $\varepsilon=l/L$ is the ratio between the persistence length of the distortional elasticity interaction and L,

$$Re=\rho\frac{VL}{\eta_s+\nu\xi_r},\quad \gamma=\frac{\nu\xi_r}{\eta_s+\nu\xi_r}.$$

We choose the nonlocal interaction function B as

$$B(\mathbf{x},\mathbf{m},\mathbf{x}',\mathbf{m}',t)=U_0\frac{1}{\varepsilon^d}g(\frac{\mathbf{x}-\mathbf{x}'}{\varepsilon})|\mathbf{m}\times\mathbf{m}'|^2,\quad\forall\mathbf{x},\mathbf{x}'\in\Omega. \tag{2.10}$$

Here d is the spatial dimension, and $g(\mathbf{x})$ is the smoothing of the delta function, which satisfies

$$g(\mathbf{x})\geq 0,\ g(\mathbf{x})=0,\ \text{when}\ \|\mathbf{x}\|\geq 1\ \text{and}\ \int_{\|\mathbf{x}\|<1}g(\mathbf{x})d\mathbf{x}=1.$$

2.2 Boundary condition

The orientation of the director on the boundaries, the so-called **anchoring condition** can be controlled by chemical treatment, or rubbing the surface of the containers [1]. To ensure the anchoring condition, we add a boundary potential to the system,

$$\tilde{U}(\mathbf{x},\mathbf{m},t)=k_BT\int_{\partial\Omega}\int_{|\mathbf{m}'|=1}\tilde{B}(\mathbf{x},\mathbf{m};\mathbf{x}',\mathbf{m}')\tilde{f}(\mathbf{x}',\mathbf{m}',t)d\mathbf{m}'d\mathbf{x}', \tag{2.11}$$

where $\tilde{f}(\mathbf{x}',\mathbf{m}',t)$ is the pdf of the boundary molecules, which were anchored at the boundary surface, $\tilde{B}(\mathbf{x},\mathbf{m};\mathbf{x}',\mathbf{m}')$ is the interaction potential function between LCP molecules and boundary molecules. Similar to potential function B, we choose

$$\tilde{B}(\mathbf{x},\mathbf{m};\mathbf{x}',\mathbf{m},t)=\tilde{U}_0\frac{1}{\tilde{\varepsilon}^{d-1}}\tilde{g}(\frac{\mathbf{x}-\mathbf{x}'}{\tilde{\varepsilon}})|\mathbf{m}\times\mathbf{m}'|,\quad\forall\mathbf{x}\in\Omega,\ \mathbf{x}'\in\partial\Omega, \tag{2.12}$$

where the function $\tilde{g}$ is the smoothing function in the $d-1$ dimensional space. Assume the direction of anchoring at the boundary point $\mathbf{x}'$ is $\mathbf{m}_b(\mathbf{x}')$, and $\tilde{f}$ is the delta function of $\mathbf{m}_b$,

$$\int_{\|\mathbf{m}'\|=1} |\mathbf{m}\times\mathbf{m}'|^2 \tilde{f}(\mathbf{x}',\mathbf{m}',t)d\mathbf{m}' = |\mathbf{m}\times\mathbf{m}_b|^2,$$

so the boundary potential can be specified as

$$\tilde{U}(\mathbf{x},\mathbf{m},t) = \tilde{U}_0 \int_{\partial\Omega} \frac{1}{\tilde{\varepsilon}^{d-1}} \tilde{g}\left(\frac{\mathbf{x}-\mathbf{x}'}{\tilde{\varepsilon}}\right) |\mathbf{m}\times\mathbf{m}_b|^2 d\mathbf{x}'. \tag{2.13}$$

We can alter the strength of the anchoring and the anchoring angles by modifying $\tilde{U}_0$ and $\mathbf{m}_b$. We replace the potential $U(\mathbf{x},\mathbf{m},t)$ in the Smoluchowski equation by

$$U^t = U + \tilde{U}.$$

For the mass conservation of the molecules (i.e. $\int_\Omega \int_{|\mathbf{m}|=1} f(\mathbf{x},\mathbf{m},t)d\mathbf{m}d\mathbf{x}=1$), we integrate both sides of the Smoluchowski equation, and obtain:

$$\begin{aligned} &\frac{\varepsilon^2}{De}\int_{|\mathbf{m}|=1}\int_{\partial\Omega}\Big\{[D_\parallel \mathbf{mm} + D_\perp(\mathbf{I}-\mathbf{mm})]\cdot(\nabla f + f\nabla U^t)\Big\}\cdot\mathbf{n}d\mathbf{x}d\mathbf{m} \\ =&\frac{d}{dt}\int_\Omega\int_{|\mathbf{m}|=1} f d\mathbf{m}d\mathbf{x} = 0. \end{aligned}$$

We take the boundary condition of the Smoluchowski equation as

$$\Big\{[D_\parallel \mathbf{mm} + D_\perp(\mathbf{I}-\mathbf{mm})]\cdot(\nabla f + f\nabla U^t)\Big\}\cdot\mathbf{n} = 0, \quad \mathbf{x}\in\partial\Omega. \tag{2.14}$$

3 LCPs under plane shear flow

3.1 1+2 dimensional model

We study the LCPs under plane shear flows, such as Couette flow and Poiseuille flow, which are shown in Fig. 1.

Here we consider the plane shear flow with the velocity oriented along the x axis, the gradient of the velocity oriented along the y axis and the vorticity along the z axis. The LCP molecules can rotate on the unit sphere $S^2 \in \mathcal{R}^3$, and the system is homogeneous in the direction of x and z axis. So we have

$$\begin{aligned} &\mathbf{x} = (x,y,z)^T, \quad \mathbf{v} = (u(y),0,0)^T, \quad \mathbf{m} = (\sin\theta\cos\phi, \sin\theta\sin\phi, \cos\theta), \\ &\nabla = (0,\partial_y,0)^T, \quad \nabla p = (C,p_y,0)^T, \quad \kappa = \begin{pmatrix} 0 & u_y & 0 \\ 0 & 0 & 0 \\ 0 & 0 & 0 \end{pmatrix}. \end{aligned}$$

The coupled problem (2.6)−(2.9) can be simplified as follows:

$$\frac{\partial f}{\partial t}=\frac{\varepsilon^2}{De}\partial_y\{[D_\perp(1-\sin^2\theta\sin^2\phi)+D_\parallel\sin^2\theta\sin^2\phi](f_y+fU_y^t)\}$$
$$+\frac{1}{De}\mathcal{R}\cdot(\mathcal{R}f+f\mathcal{R}U^t)-\mathcal{R}(\mathbf{m}\times\kappa\cdot\mathbf{m}f), \tag{3.1}$$
$$u_t+C=\frac{1-\gamma}{Re}u_{yy}+\frac{\gamma}{ReDe}\partial_y\tau_{12}, \tag{3.2}$$
$$\tau_{12}=3\langle m_1m_2\rangle-\langle m_2^2\mathcal{R}_zU^t-m_2m_3\mathcal{R}_yU^t\rangle+\frac{De}{2}u_y\langle m_1^2m_2^2\rangle. \tag{3.3}$$

For Couette flow, the constant $C=0$, and the boundary conditions of Navier-Stokes type equations (3.2), (3.3) are $u(0)=0$, $u(1)=1$. For Poseuille flow, the constant $C\neq0$, with the fixed boundary conditions $u(0)=u(1)=0$.

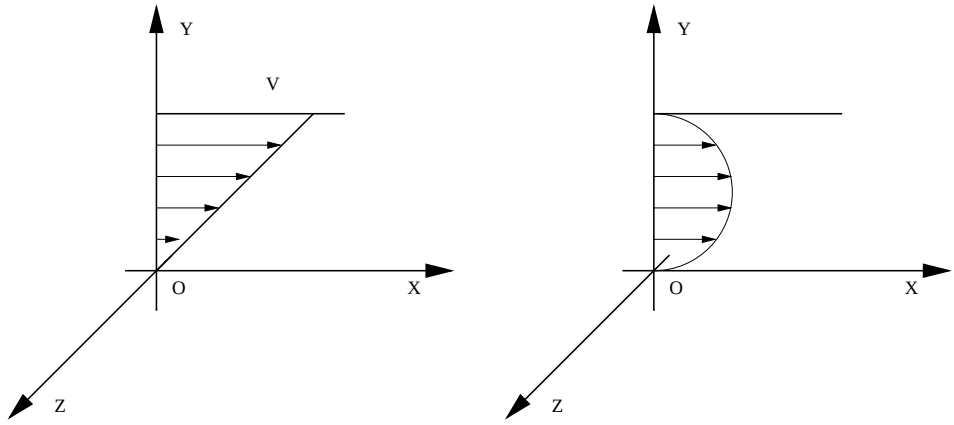

Figure 1: Plane shear flow: flow velocity $\vec{v}=(u(y),0,0)$ along the x axis, flow gradient along the y axis and vorticity along the z axis. Left is the Couette flow, no pressure gradient, upper plate moving; right is the Poiseuille flow, pressure gradient $\partial p/\partial t$ with both plates fixed.

3.2 Numerical scheme

In the Smoluchowski equation (3.1), the probability density function (pdf) f depends on the orientational variable $\mathbf{m}$ and the spatial variable y. So it is a three-dimensional problem. For smooth pdf f, the spectral method is a good choice to discretize the problem. We expand $f(y,\mathbf{m},t)$ in a series of spherical harmonic functions Y_l^m as

$$f(y,\mathbf{m},t)=\frac{\rho(y,t)}{4\pi}+\sum_{l=2,\ even}^{\infty}\sum_{m=-l}^{l}b_{lm}(y,t)Y_l^m(\theta,\phi), \tag{3.4}$$

where b_{lm}'s are complex functions of time and location and $\rho(y,t)$ is the density of molecules at the location y. Since the orientational distribution function is real, the fol-

lowing property is true:

$$b_{l-m}=(-1)^m b_{lm}^*,$$

where the asterisk represents the conjugation operation. In the expansion equation (3.4), the subscript l takes only even values since a reflection of the space $(\theta,\phi)\to(\pi-\theta,\phi+\pi)$ leaves f unchanged (i.e. the molecules don't distinguish head and tail).

With Eq. (3.4), we have

$$\begin{aligned}
&m_1^2=C_1(Y_2^2+Y_2^{-2})-C_0Y_2^0+\frac{1}{3},\\
&m_2^2=-C_1(Y_2^2+Y_2^{-2})-C_0Y_2^0+\frac{1}{3},\\
&m_3^2=2C_0Y_2^0+\frac{1}{3},\quad m_1m_2=iC_1(Y_2^{-2}-Y_2^2),\\
&m_1m_3=C_1(Y_2^{-1}-Y_2^1),\quad m_2m_3=iC_1(Y_2^{-1}+Y_2^1),
\end{aligned}$$

with coefficients $C_1=\sqrt{2\pi/15}$ and $C_0=\frac{2}{3}\sqrt{\pi/5}$. The second moment tensor $\langle\mathbf{mm}\rangle$ can be specified by spherical harmonic coefficients $\{b_{2s}(y,t)\}_{s=-2,\cdots,2}$ as

$$\begin{aligned}
&\langle m_1^2\rangle=2C_1\Re(b_{22}(y,t))-C_0b_{20}(y,t)+\rho(y,t)/3,\\
&\langle m_2^2\rangle=-2C_1\Re(b_{22}(y,t))-C_0b_{20}(y,t)+\rho(y,t)/3,\\
&\langle m_1m_2\rangle=2C_1\Im(b_{2-2}(y,t)),\\
&\langle m_1m_3\rangle=2C_1\Re(b_{2-1}(y,t)),\\
&\langle m_2m_3\rangle=2C_1\Im(b_{2-1}(y,t)).
\end{aligned}$$

Here, $\Re(b_{\alpha\beta})$ and $\Im(b_{\alpha\beta})$ are the real and imaginary parts of $b_{\alpha\beta}$ respectively.

If we define the operator $\mathcal{L}=\mathcal{R}/i=(\mathcal{L}_x,\mathcal{L}_y,\mathcal{L}_z)$ and $\mathcal{L}_\pm=\mathcal{L}_x\pm i\mathcal{L}_y$, then the spherical harmonic functions $Y_l^m(\theta,\phi)$ have the following properties:

$$\begin{aligned}
&\mathcal{R}\cdot\mathcal{R}Y_l^m=-l(l+1)Y_l^m,\\
&\mathcal{L}_zY_l^m=mY_l^m,\\
&\mathcal{L}_\pm Y_l^m=\sqrt{(l\mp m)(l\pm m+1)}Y_l^{(m+1)}.
\end{aligned}$$

We choose the smoothing functions g and $\tilde{g}$ as

$$g(y)=\begin{cases}\frac{1}{Z}e^{\frac{1}{y^2-1}}, & |y|<1,\\ 0, & \text{otherwise},\end{cases}\qquad \tilde{g}(y)=\begin{cases}e^{\frac{y^2}{y^2-1}}, & |y|<1,\\ 0, & \text{otherwise},\end{cases}$$

where Z is the normalization constant. Then the excluded volume potential and the

boundary potential can be expanded as

$$\begin{aligned}
U(y,\mathbf{m},t) &= \frac{2U_0}{3} g_\varepsilon * \rho(y,t) - \frac{8\pi U_0}{15} \sum_{s=-2}^{2} g_\varepsilon * b_{2s}(y,t) Y_2^s(\theta,\phi),\\
\tilde{U}(y,\mathbf{m},t) &= \tilde{U}_0 \tilde{g}_\varepsilon(y)\rho(y,t)|\mathbf{m}\times\mathbf{m}_0|^2\\
&= \frac{2\tilde{U}_0}{3}\tilde{g}_\varepsilon(y-y_b)\rho(y,t) - \tilde{U}_0\tilde{g}_\varepsilon(y-y_b)\rho(y,t)\sum_{s=-2}^{2} C_{2s}(\mathbf{m}_0)Y_2^s(\theta,\phi),
\end{aligned}$$

where $g_\varepsilon(y)=\frac{1}{\varepsilon}g(\frac{y}{\varepsilon})$, $\tilde{g}_{\tilde{\varepsilon}}(y)=\tilde{g}(\frac{y}{\tilde{\varepsilon}})$, $g*f$ denote the convolution of the functions g and f, and C_{2s}'s are given by

$$\begin{aligned}
&C_{2-2}(\mathbf{m}) = \sqrt{\frac{2\pi}{15}}(m_1+im_2)^2, \quad C_{2-1}(\mathbf{m}) = 2\sqrt{\frac{2\pi}{15}}m_3(m_1+im_2),\\
&C_{20}(\mathbf{m}) = \frac{2}{3}\sqrt{\frac{\pi}{5}}(3m_3^2-1), \quad C_{21}(\mathbf{m}) = -2\sqrt{\frac{2\pi}{15}}m_3(m_1-im_2),\\
&C_{22}(\mathbf{m}) = \sqrt{\frac{2\pi}{15}}(m_1-im_2)^2.
\end{aligned}$$

The stress tensor of polymers can be specified,

$$\begin{aligned}
\tau_{12}^{(p)} = &-6\sqrt{\frac{2\pi}{15}}\Im(b_{22}(y,t)) - \left\langle i\left[-\sqrt{\frac{2\pi}{15}}(Y_2^{-2}+Y_2^2) - \frac{2}{3}\sqrt{\frac{\pi}{5}}Y_2^0 + \frac{1}{3}\right]L_z U^t\right.\\
&\left. - \frac{i}{2}\sqrt{\frac{2\pi}{15}}(Y_2^{-1}+Y_2^1)(L_+-L_-)U^t\right\rangle\\
&+\frac{Deu_y}{2}\left(\frac{\rho(y,t)}{15} - \frac{2}{3}\sqrt{\frac{2\pi}{35}}\Re(b_{44}(y,t)) + \frac{2\sqrt{\pi}}{105}b_{40}(y,t) - \frac{4}{21}\sqrt{\frac{\pi}{5}}b_{20}(y,t)\right), \qquad (3.5)
\end{aligned}$$

and the following relationship is used to calculate the average term $\langle(\cdot)\rangle$ above:

$$Y_2^p Y_l^m = \sqrt{\frac{15}{2\pi}}(b_{l-}^{p,m}Y_{l-2}^{p+m} + b_l^{p,m}Y_l^{m+p} + b_{l+}^{p,m}Y_{l+2}^{m+p}), \quad p=-2,-1,0,1,2. \qquad (3.6)$$

This relationship was reported in Zhou et al. [21], and the constants $b_{l-}^{p,m}, b_l^{p,m}, b_{l+}^{p,m}$ were defined there. We use the second-order finite difference to discretize the derivative of the spacial variable. Then the Smoluchowski equation is translated to a system of ODEs. We use the fourth-order Runge-Kutta method to solve the ODEs. To discretize the Navier-Stokes type equation, the second-order finite difference is used for the spatial derivatives, and for the time derivative, the backward Euler method is used.

4 Numerical results

Our kinetic-hydrodynamic model includes nine parameters: the Deborah number De, ε, the dimensionless translation diffusion coefficient perpendicular and parallel to the molecular orientation $D_\perp$ and $D_\parallel$, the proportion of the polymer viscosity to total viscosity γ, the strength of the excluded volume potential U_0 and the boundary potential $\tilde{U}_0$, the Reynolds number Re and the direction of anchoring $\mathbf{m}_b$. Here we vary the parameters De and ε, and fix the others as follows. We specify $Re=1.0$ to produce laminar flow. Because the isotropic to nematic phase transition was predicted for homogeneous flow at $U_0\approx 6.731393$ and $U_0=7.5$ [22], we choose $U_0=8.0$ to assure nematic phase, and $\gamma=0.9, D_\perp=0.1, D_\parallel=0.2$ for dilute solution. The tangential anchoring condition (i.e., $\mathbf{m}_b=(1,0,0)$) was chosen, and $\tilde{U}_0=2U_0$ to ensure anchoring. We use the uniform mesh to discretize the spatial variable $y\in[0,1]$ and choose the mesh, which satisfies $\varepsilon/h\geq 5$, to ensure the precision of the convolution.

4.1 Flow modes

We classify our results into two categories, in-plane phase and out-of-plane phase, according to the dynamics of the directors.

In-plane phases: All the directors remain in the shear plane, so they can be simplified as $\mathbf{n}=(n_1,n_2,0)$. For the normalization of $\mathbf{n}$, we only show the dynamics of the second component n_2 in Fig. 2. We get five types of in-plane flow modes, in-plane elastic driven steady state (IE), in-plane viscous driven steady state (IV), in-plane tumbling-wagging composite state (IT), in-plane discrete tumbling-wagging composite state (IDT) and in-plane wagging state (IV). Four flow modes, IE, IV, IT and IW, were reported by Rey et al. [19] using the complete closure model. Using 1+1 kinetic model, Yu et al. [20] simulated all five flow modes. By incorporating a spacial diffusion term in our 1+2 model, we also get all five flow modes:

• In-plane elastic driven steady state (IE): This planar steady state arises due to the long range order elasticity stored in the spatial deformed pdf field. There is no orientation boundary layer for the absence of flow-alignment in the bulk region (see Fig. 2(a)).

• In-plane viscous driven steady state (IV): In this steady mode, the director profile shows a flow aligning bulk region and two boundary layers. The director rotates from the aligning angle to the anchoring angle on traversing the boundaries (see Fig. 2(e)).

• In-plane tumbling-wagging composite state (IT): In this periodic planar mode the directors rotate in the bulk region or oscillate in the boundary layers periodic (see Fig. 2(b)). The boundary between the tumbling region and each boundary layer is characterized by the periodically emergence of the abnormal nematic state (also c.f. [19,23]), where the order parameters are negative. Because of the spacial transportation and long-term order interaction, the configurations are biaxial.

• In-plane discrete tumbling-wagging composite state (IDT): In this periodical in-plane mode, tumbling-wagging phase in the bulk region are separated by flow aligning

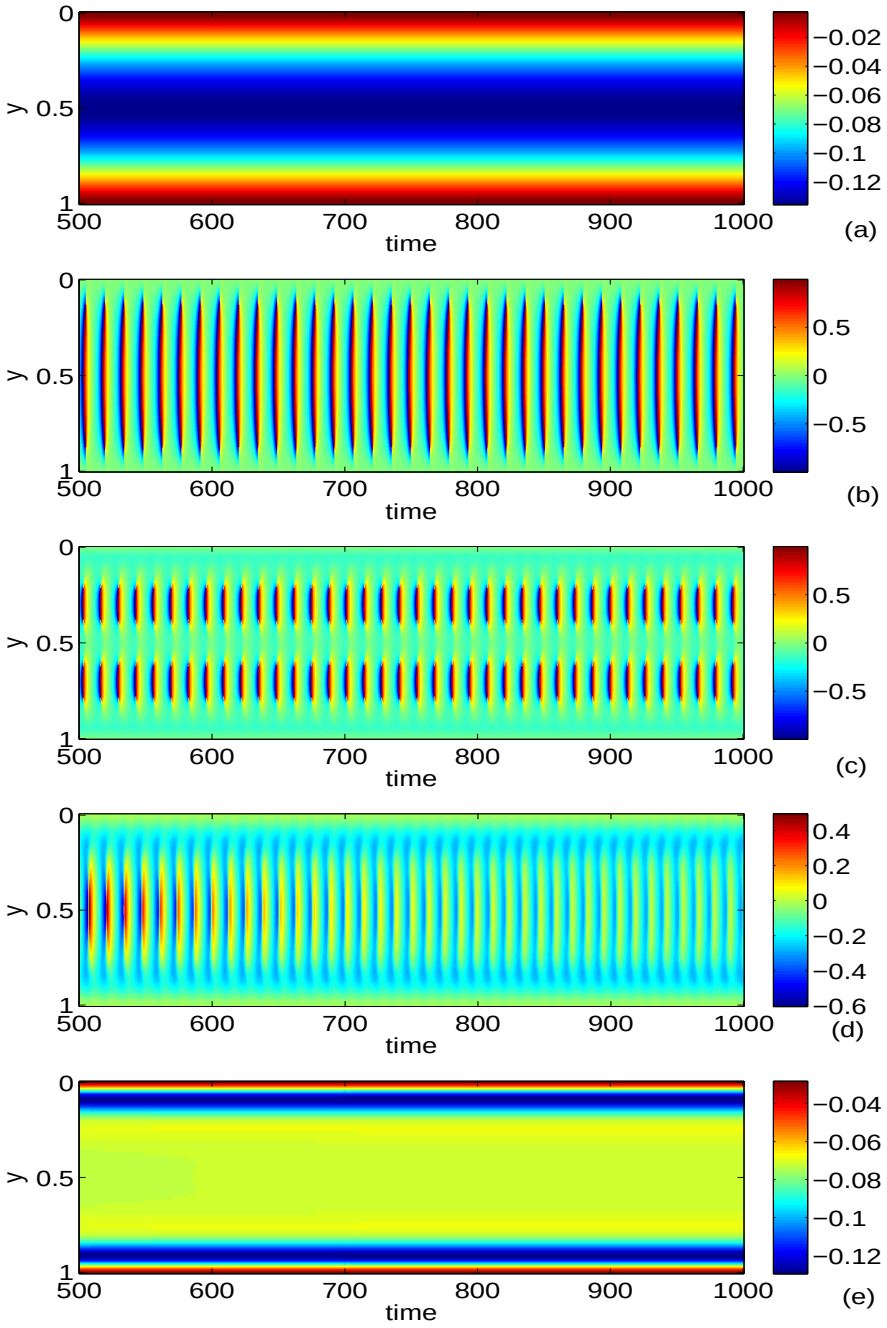

Figure 2: The dynamics of the second component of director n_2, the x axis is the evolution of time, and the y axis is spacial location. From top to bottom, parameters are (a) $De=0.1,\varepsilon=0.08$; (b) $De=0.1,\varepsilon=0.04$; (c) $De=2.5,\varepsilon=0.04$; (d) $De=2.25,\varepsilon=0.08$; (e) $De=4.5,\varepsilon=0.08$ respectively.

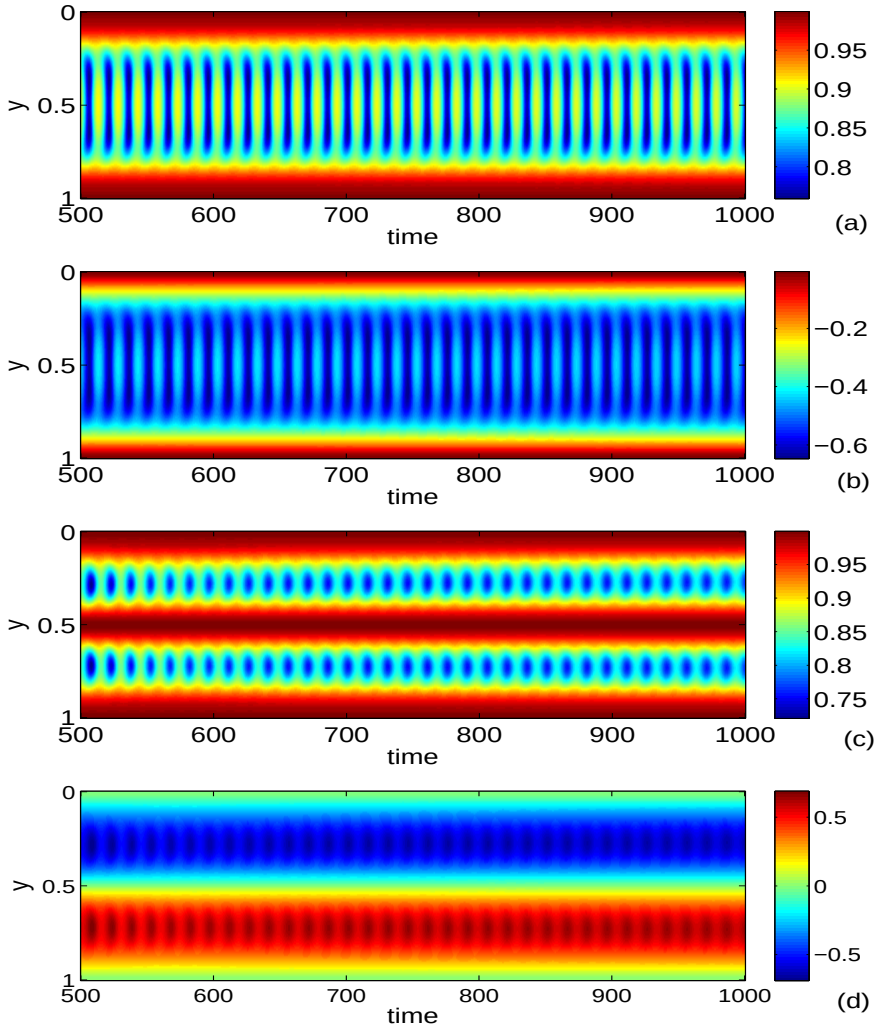

Figure 3: Out-of-plane kayaking. The color describes the values of the first (a, c) and third (b, d) component of directors, the x axis is the evolution of time and the y axis is the spatial location $y\in[0,1]$. The parameters are $De=5.0,\varepsilon=0.04$.

phase. The director dynamics behave like IT in each local area (see Fig. 2(c)).

• In plane wagging state (IW): In this mode, the director dynamics over the entire flow geometry is wagging with an amplitude that decreases from a maximum at the centerline to the two boundaries (see Fig. 2(d)).

Out-of-plane phase: In addition to the five in-plane flow modes, we also simulated eight out-of-plane flow modes. In this category, parts of directors came out of the shear plane occasionally (e.g. OTP, OTC) or stayed out of the shear plane permanently (e.g. OEA, OEC1, OEC2).

• Out-of-plane kayaking (OK): In this mode, the directors oscillate out of the shear

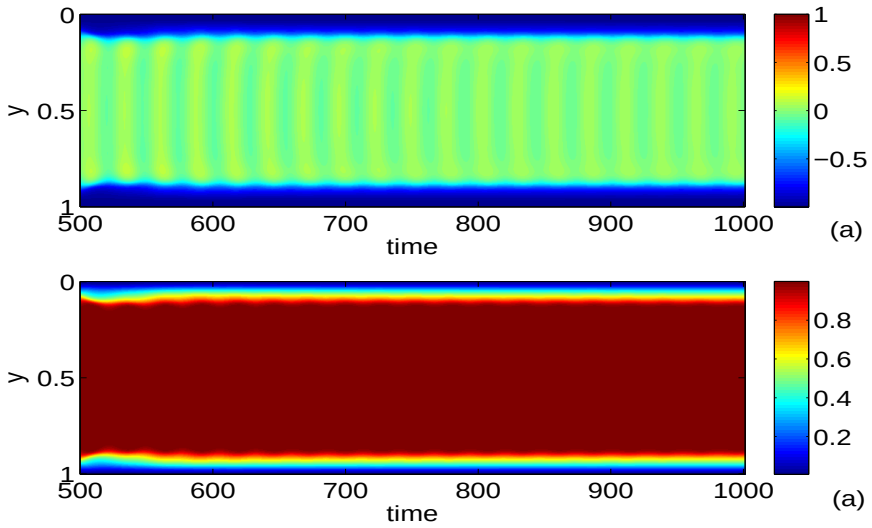

Figure 4: Out-of-plane elastic driven steady state (OEA). The parameters are $De=2.0$,$\varepsilon=0.02$. The top figure is the first component of the director n_1 and the bottom is the third component of the director n_3.

plane periodically, which is called kayaking. Similar to IDT mode, the bulk region can be divided into several independent kayaking domains, and the directors of two adjacent kayaking domains are axisymmetric about the their interface. If the value of ε is decreased, the number of individual kayaking regions will increase. The dynamics of the first and third components of the directors are shown in Fig. 3.

• Out-of-plane elastic-driven steady state with achiral structure (OEA): In this mode, the director shows steady twist structures and the twist angles are symmetric with respect to the centerline. The steady state arises due to the long range order elasticity, which is predicted by the Leslie-Ericksen theory. We can see in the Fig. 4, the net director twist rotation is nil from the top boundary to bottom.

• Out of plane elastic-driven steady state with chiral structure (OEC1): In this out-of-plane mode, the director shows steady twist structures, with π radian difference between the anchoring angles at the top and button boundary, but present no defects or disclinations (see Fig. 5(a,b)).

• Out-of-plane elastic-driven steady state with chiral structure (OEC2): In this out-of-plane mode, the director shows steady twist structures, with 2π radian difference between the anchoring angels at the top and button boundary, but present no defects or disclinations (see Fig. 5(c,d)).

• In-plane tumbling-wagging coupled with out-of-plane steady state (ITOE1, ITOE2): In these two modes, three in plane tumbling-wagging states were separated by two out of plane steady state. For ITOE1 (see Fig. 6(a, b)), the directors leave the shear plane in the same direction, and they mirror symmetry about the normal face on the centerline. For ITOE2 (see Fig. 6(c, d)), the directors leave the shear plane in the opposite direction,

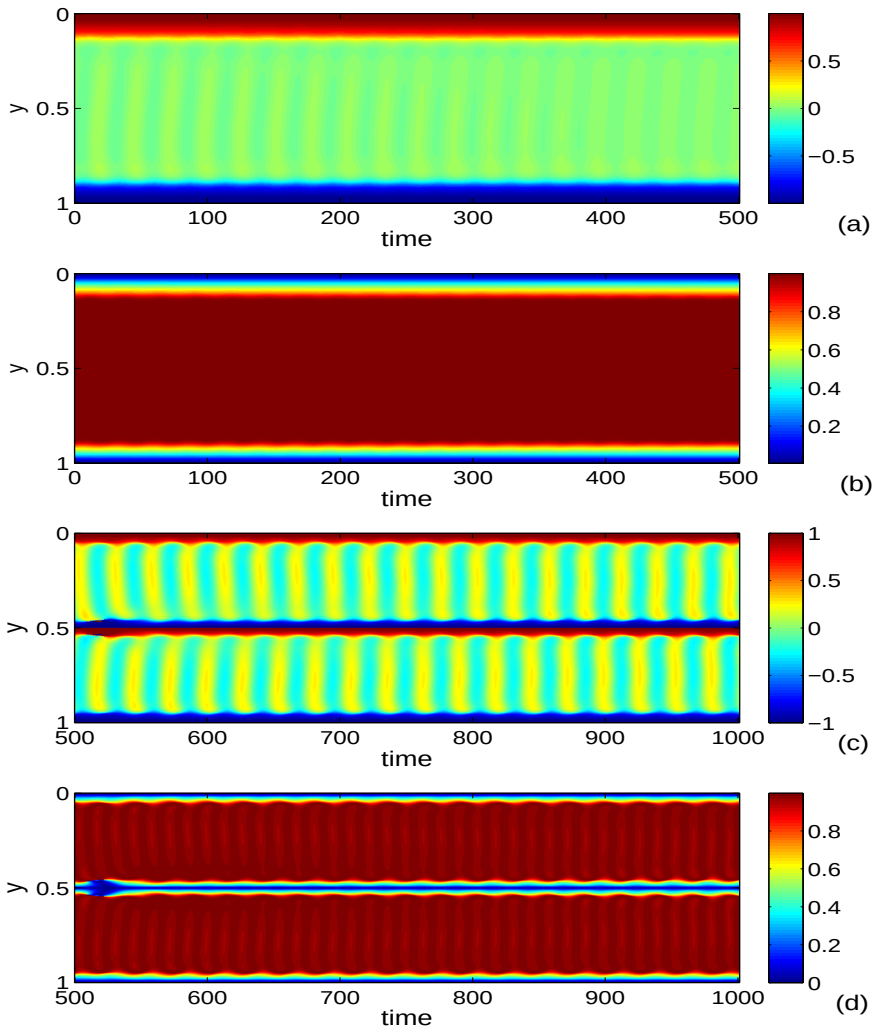

Figure 5: Out-of-plane elastic driven steady state. The parameters are $De=2.0, \varepsilon=0.01$. (a, b)/(c, d) describe OEC1/OEC2 respectively. The figures denote the first (a, c) and the third (b, d) components of the director.

and they are axisymmetric about the centerline.

• Out-of-plane tumbling-wagging composite state with periodic chirality (OTP): In the bulk region, the directors rotate periodically (tumbling), and in the boundary layer, the directors present out-of-plane oscillation (see Fig. 7(a, b)). The directors at both boundary layers oscillates on the same side of the shear plane.

• Out-of-plane tumbling-wagging composite state with π chiral structure (OTC): In the bulk region, the directors rotate periodically(tumbling), and in the boundary layers, the directors present out of plane oscillation (see Fig. 7(c, d)). The directors at both boundary layers oscillates at the opposite side of shear plane.

We simulated all eight out-of-plane flow modes: OEA, OEC1, OEC2, OTC, OTP, OK,

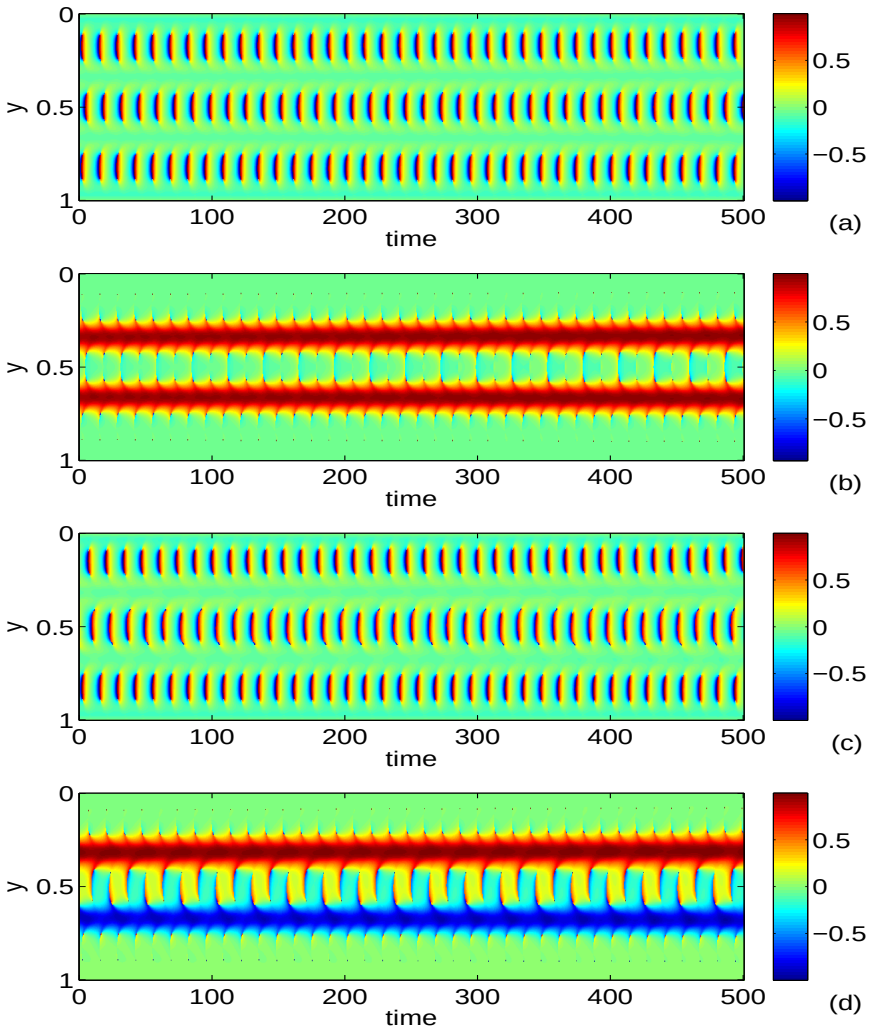

Figure 6: In-plane tumbling-wagging composite out-of-plane steady state. The x axis is the evolution of time and the y axis is the location of spatial in $[0,1]$, the parameters are $De=2.0,\varepsilon=0.02$. (a)-(b) show the ITOE1 flow mode and (c)-(d) show the ITOE2 flow mode.

ITOE1, ITOE2. The first five have been reported by Rey et al. [19], and the last three are new modes.

4.2 Dynamics of defects

Defects are a very important aspect of the microstructure in the LCPs flow. Defects arise in the region where the director dynamics conflict with their neighbors, and connect two conflicting phases like a bearing. For example, if the tumbling rates of neighboring LCPs are different, or a tumbling region is connected with wagging region, defects will arise.

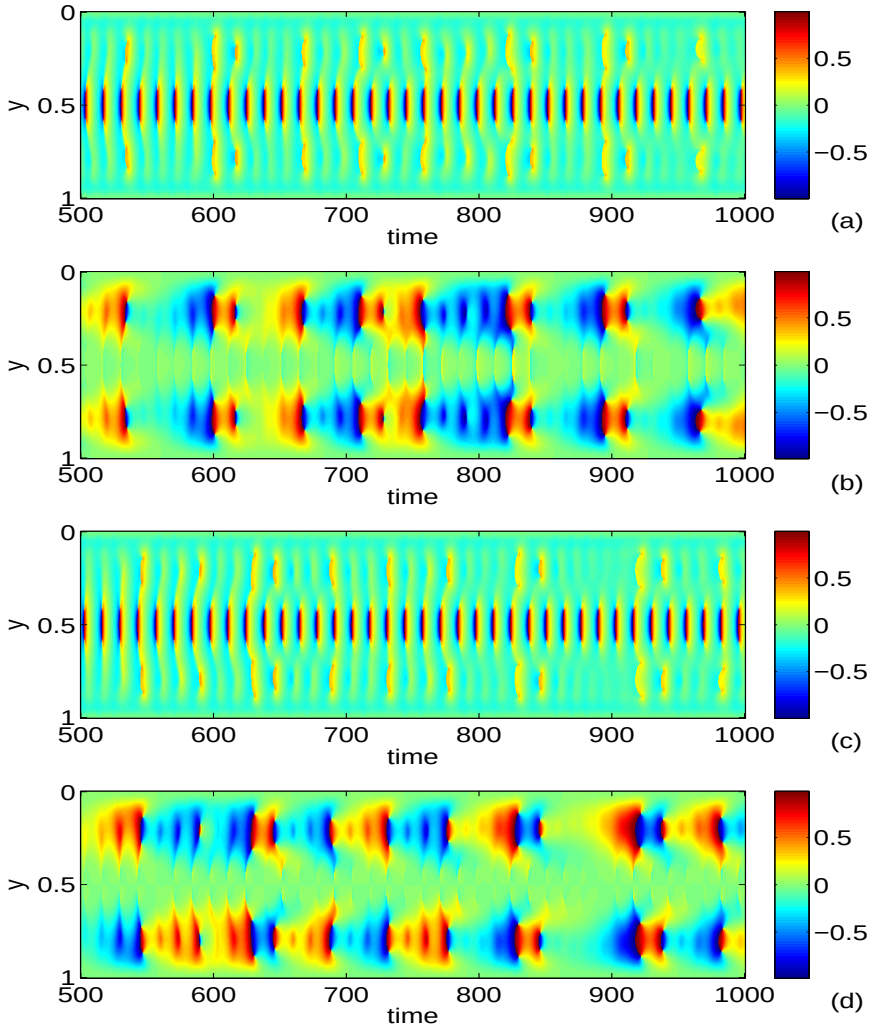

Figure 7: The director dynamics of OTP and OTC. The axis is the evolution of time, the y axis is the spatial location. (a) and (b) show the dynamics of OTP ; (c) and (d) show the dynamics of OTC; The parameters are $De=3.0$,$\varepsilon=0.04$, (a),(c) show the evolution of second component of directors and (b),(d) show the evolution of third component of directors.

The order parameter is about zero at the defects (see Fig. 8(c)), and the minimum of the excluded volume potential is larger than that in the normal nematic state. This causes a decrease in density in the defect core (see Fig. 8(b)). Defects also introduce big stress variation (see Fig. 8(d)), which causes the shear rate to increase (see Fig. 8(e)).

4.3 Weak shear results

For weak shear and low Ericksen number conditions, Forest et al. [12] studied the tensor model using asymptotic analysis, and got the scaling properties of order parameters and

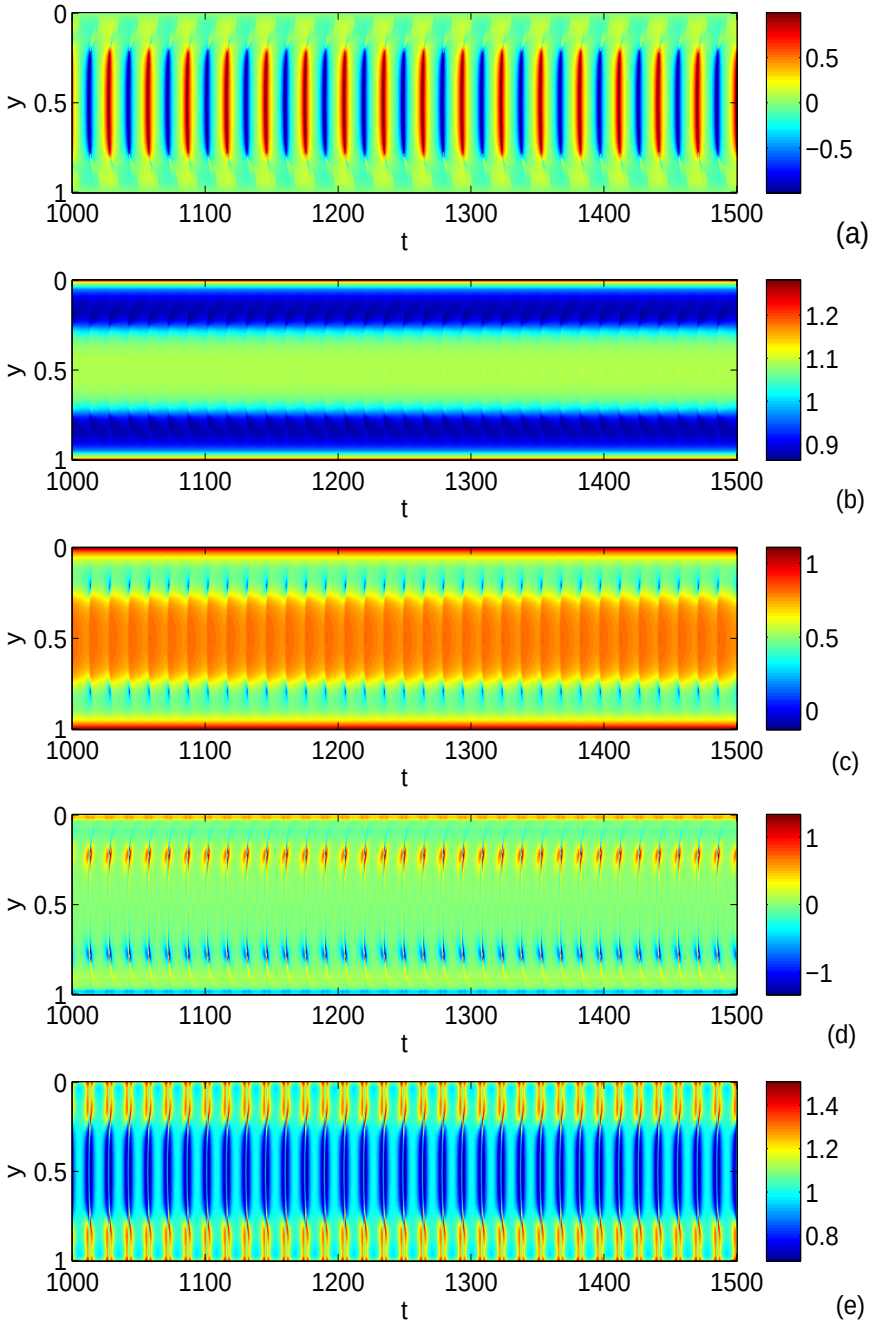

Figure 8: The dynamics of defects. From top to buttom, the graphs show the second component of director, density, order parameter, velocity and shear rate respectively. The parameters are $De=1.0,\varepsilon=0.04$.

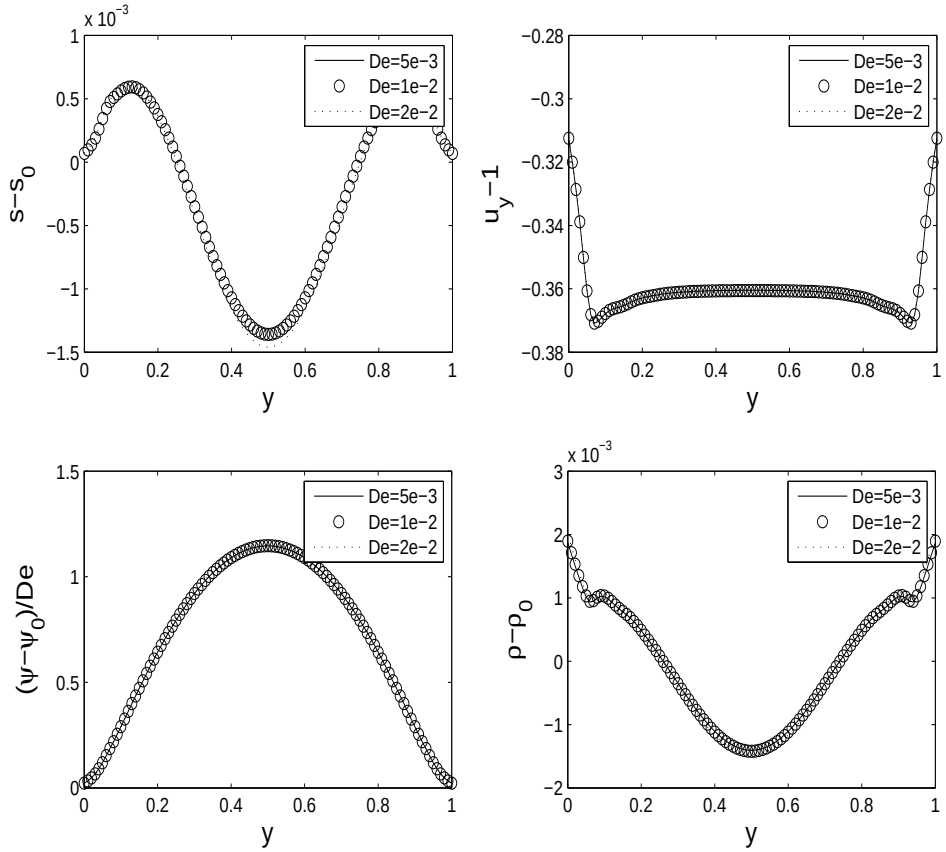

Figure 9: Tangential anchoring condition. The parameters are $U=8.0, \varepsilon=0.08$. From left to right top to buttom, the graphs show order parameters, shear rate, LE angle and density respectively.

Leslie angles as $s=s_0+De^2 s_2+\mathcal{O}(De^3)$, $\beta=\beta_0+De^2\beta_2+\mathcal{O}(De^3)$, $\psi=\psi_0+De\psi_1+\mathcal{O}(De^2)$ for tangential ($\psi_0=0$) and homeotropic ($\psi_0=\frac{\pi}{2}$) anchoring. Zhou et al. [21] verified it numerically, and Yu et al. [20] replicated those results using 1+1 kinetic model for tangential anchoring condition, but not for homeotropic anchoring condition.

In our simulations, we let $De=0$ to get s_0, β_0, ψ_0 and initial pdf for weak shear condition. Our results are consistent with those of [12] except for the order parameters for tangential anchoring condition. For tangential anchoring condition, the order parameter only has the property like $s=s_0+\mathcal{O}(De)$, and β is almost zero.

4.4 Some results of pressure driven flow

For completeness, we also simulate some results under pressure driven flow. Here let the dimensionless driven pressure gradient $C=-4(1-\gamma)/Re$. In Fig. 11, we show the dynamics of the second component of the directors **n** under the parameters $\varepsilon=0.08, De=0.1$ and $De=5.0$ and $\varepsilon=0.02, De=1.0$.

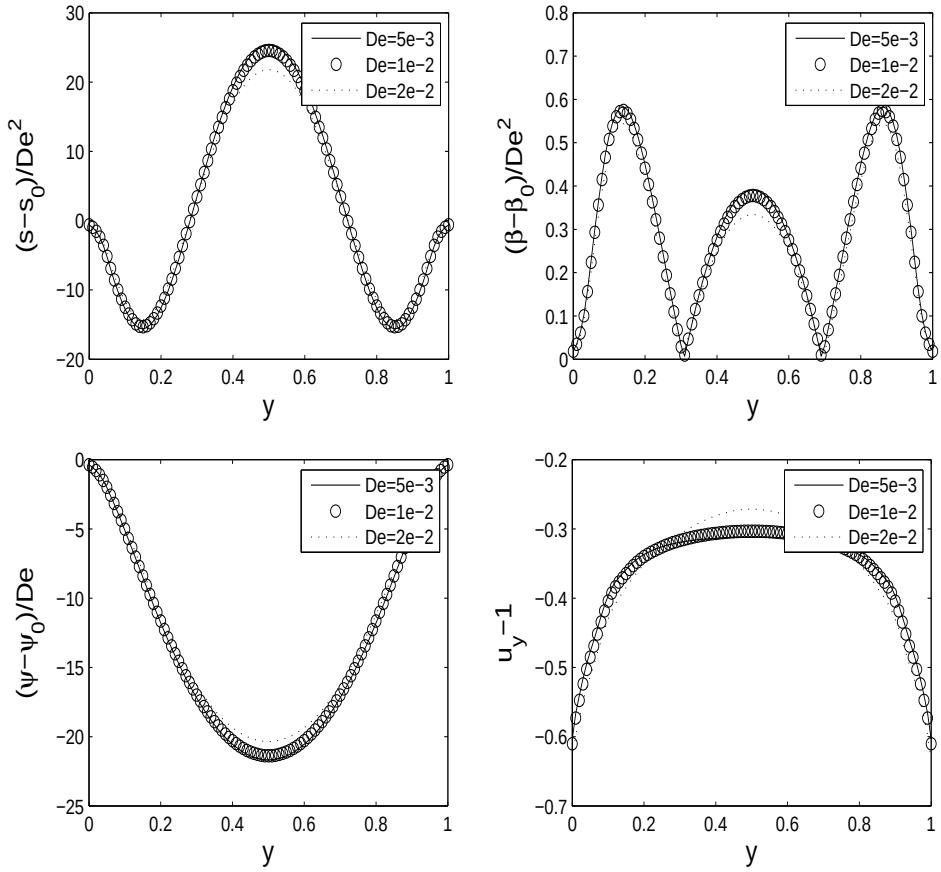

Figure 10: Perpendicular anchoring condition. The parameters are $U=8.0, \varepsilon=0.08$. From left to right top to buttom, the graphs show oder parameter s, β, LE angle and shear rate respectively.

4.5 Compare with Bingham closure

In high-dimensional cases, the simulation of the kinetic model becomes time consuming. Reduced equations with respect to the moments of probability distribution function (pdf) can be obtained from kinetic models. However, the equations of lower-order moments of pdf involved higher-order moments. To close these equations, higher-order moments must be evaluated by lower-order moments, which is called closure approximation.

Closure approximations for complex fluids have been investigated for many years. Various closure approximations have been proposed, including Doi's quadratic closure [24], the HL closure [25], the orthotropic closure [26], and the Bingham closure [27]. Feng et al. [28] compared five commonly used closures methods numerically and found that the Bingham closure behaves better than others, although it deviates from the solutions of original kinetic theory when shear rate and nematic potential strength are both very large. The Bingham closure is a particular case of quasi-equilibrium closure approxima-

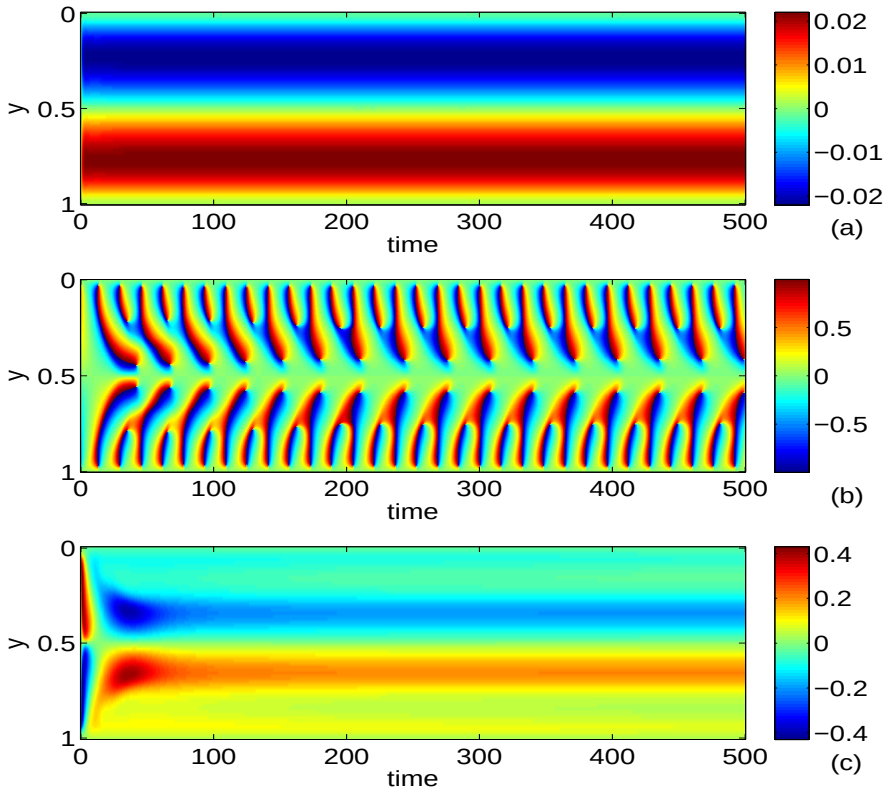

Figure 11: The second component of the directors. The x axis denote the time evolution and y axis is the spatial location in interval $[0,1]$. And the parameters are (a) De=0.1,ε=0.08; (b) De=1.0,ε=0.02; (c) De=5.0,ε=0.08.

tion (QEA) in rod-like polymers. The systemic depiction of QEA are given by Gorban and coworkers [29,30]. Ilg et al. [31] applied QEA to flexible polymers in homogeneous system, while Ilg et al. [32] analyzed rod-like polymers, and proved validity of energy dissipation for homogeneous systems when flow is absent. Yu et al. [33] applied the Bingham closure to LCPs in nonhomogeneous systems and developed a relatively simple but general nonhomogeneous kinetic model for LCPs as well as efficient reduced moment models that maintain energy dissipation.

In Table 1, we compare our simulation results using the 1+2 dimensional kinetic model with Rey's results [19], the results of 1+1 dimensional kinetic model [20] and the Bingham closure model [33]. All the in-plane flow modes can be simulated by all four models, with the exception that the complete closure model does not find IDT because of the absence of spatial transportation. The out-of-plane flow modes are more complex. The two closure models failed to simulate all the out-of-plane results, such as ITOE1 and ITOE2 were not simulated by both closure models and OK was not simulated by the complete closure model. However, for the strong nonlinearity, the solutions are tied up to initial data and the parameters. Perhaps new combinations of initial data and the

Table 1: Comparison of the results of four different models: 1+2 and 1+1 dimensional kinetic model, Bingham closure model and the complete closure model used by Rey et al. [19]. The first column list the flow modes, defined in Section 4.1, and Y means this type of flow mode can be simulated by the model, and N means the flow mode was not simulated by the model or the simulation was not reported in [19].

Flow Mode	1+2	1+1	Bingham	Complete
IE	Y	Y	Y	Y
IT	Y	Y	Y	Y
IDT	Y	Y	Y	N
IW	Y	Y	Y	Y
IV	Y	Y	Y	Y
OEA	Y	N	Y	Y
OEC1	Y	N	Y	Y
OEC2	Y	N	Y	Y
OTP	Y	N	Y	Y
OTC	Y	N	Y	Y
OK	Y	N	Y	N
ITOE1	Y	N	N	N
ITOE2	Y	N	N	N

parameters in the simulations of closure models would generate them. On the other hand, in the complete closure model, the spatial transportation is absent, and the potential (Marrucci Greco potential) is a special case of the kernel type potential used in the Bingham closure model. So it is reasonable that the Bingham closure model performed better. In summary, numerical results show that Bingham closure is reliable in simulating the dynamics of LCPs.

5 Conclusion

We introduced a kinetic-hydrodynamic coupled model for dilute LCPs solution for inhomogeneous systems by using a kernal type potential and a boundary potential, and we applied it to 1+2 dimensional case. Using the spherical harmonic expansion to reduce computational complexity, we replicated results of five in-plane flow modes: in-plane elastic driven steady state, in-plane tumbling and wagging composite state, in-plane wagging, in-plane discrete tumbling and wagging and in-plane viscous driven steady state. We also simulated many more out of plane flow modes, including out of plane tumbling-wagging composite state with periodic chirality, out of plane tumbling-wagging composite state with π and 2π chiral structure, out of plane elastic-driven steady state with achiral structure, out of plane elastic-driven steady state with chiral structure, out of plane kayaking and in plane tumbling-wagging coupled with out of plane steady state. In addition to demonstrating the ability of our model to simulate

the dynamics of LCPs, we showed that it successfully describes the dynamics of defects and replicates some of weak shear limit results. Finally, we compare two kinetic models with two closure models, and the result shows that the Bingham closure model, which maintains energy dissipation, is a reliable approximation to the kinetic model.

Acknowledgments

The authors would like to thank Prof. Sharon Murrel for her help in revising the English. Guanghua Ji is partially supported by the National Science Foundation of China 10726015. Pingwen Zhang is partially supported by the special funds for Major State Research Projects 2005CB321704 and National Science Foundation of China for Distinguished Young Scholars 10225103 and 20490222.

References

[1] P. de Gennes and J. Prost, The Physics of Liquid Crystals, 2nd edition, Oxford University, New York (1993).
[2] F. Leslie, Advances in Liquid Crystals, 4, (1979), pp. 1–81.
[3] M. Doi and S. Edwards, The Theory of Polymer Dynamics, Clarendon Press, Oxford (1986).
[4] G. Hand, J. Fluid Mech., 13, (1962), pp. 33–46.
[5] A. Beris and B. Edwards, Theomodynamics of flowing systems with internal microstructure, Oxford Science Publications, New York (1994).
[6] T. Tsuji and A. D. Rey, J. Non-Newtonian Flow Mech., 73, (1997), pp. 127–152.
[7] G. Marrucci and P. Maffettone, Macomolecules, 22, (1989), pp. 4076–4082.
[8] R. Larson, Macomolecules, 23, (1990), pp. 3983–3992.
[9] R. Larson and H. Öttinger, Macomolecules, 24(23), (1991), pp. 6270–6282.
[10] R. Nayak, Molecular Simulation of Liquid Crystal Polymer Flow: A Wavelet-Finite Element Analysis, Ph.D. Thesis, MIT (1998).
[11] V. Faraoni, M. Grosso and S. Crescitelli, J. Rheol., 43(3), (1998), pp. 829–843.
[12] M. Forest, Q. Wang and R. Zhou, Rheol. Acta, 43(1), (2004), pp. 17–37.
[13] M. Forest, Q. Wang and R. Zhou, Rheol. Acta, 44(1), (2004), pp. 80–93.
[14] Q. Wang, J. Chem. Phys., 116, (2002), pp. 9120–9136.
[15] G. Marrucci and F. Greco, Mol. Cryst. Liq. Cryst., 206, (1991), pp. 17–30.
[16] J. Feng, G. Leal and G. Sgalari, J. Rheol., 44(5), (2000), pp. 1085–1101.
[17] Q. Wang, W. E, C. Liu and P. Zhang, Physical Review E, 65, (2002), p. 051504.
[18] W. E and P. Zhang, Methods Appl. Anal., 13(2), (2006), pp. 181–198.
[19] A. Rey and T. Tsuji, Macromol. Theory Simul., 7(6), (1998), pp. 623–639.
[20] H. Yu and P. Zhang, J. Non-Newtonian Flow Mech., 141(2-3), (2007), pp. 116–127.
[21] R. Zhou, M. Forest and Q. Wang, Multiscale Model. Simul., 3(4), (2005), pp. 853–870.
[22] H. Liu, H. Zhang and P. Zhang, Comm. Math. Sci., 3(2), (2005), pp. 201–218.
[23] S. Chandrasekhar, Liquid Crystals, Cambridge University Press, Cambridge (1977).
[24] M. Doi, J. Polym. Sci., Polym. Phys. E, 19, (1981), pp. 229–243.
[25] E. J. Hinch and L. G. Leal, J. Fluid Mech., 76, (1976), pp. 187–208.
[26] J. S. Cintra and C. L. Tucker, J. Rheol., 39, (1995), pp. 1095–1122.
[27] C. V. Chaubal and L. G. Leal, J. Rheol., 42, (1998), pp. 177–201.

[28] J. Feng, C. V. Chaubal and L. G. Leal, J. Rheol., 42, (1998), pp. 1095–1119.
[29] A. N. Gorban, I. V. Karlin, P. Ilg and H. C. Öttinger, J. Non-Newtonian Flow Mech., 96, (2001), pp. 203–219.
[30] A. N. Gorban, P. A. Gorban and I. V. Karlin, J. Non-Newtonian Flow Mech., 120, (2004), pp. 149–167.
[31] P. Ilg, I. V. Karlin and H. C. Öttinger, Physica A, 315, (2002), pp. 367–385.
[32] P. Ilg, I. V. Karlin, M. Kröger and H. C. Öttinger, Physica A, 319, (2003), pp. 134–150.
[33] H. Yu, G. Ji and P. Zhang, Phys. Rev. E, submitted.